Nano Energy 41 (2017) 426–433

Contents lists available at ScienceDirect

Nano Energy

journal homepage: www.elsevier.com/locate/nanoen

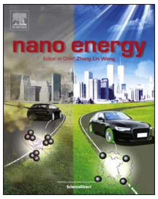

Full paper

Revisiting the origin of cycling enhanced capacity of Fe_3O_4 based nanostructured electrode for lithium ion batteries

Yuan Huang[a], Zihan Xu[a], Jiangquan Mai[a], Tsz-Ki Lau[a], Xinhui Lu[a], Yao-Jane Hsu[b], Yongsheng Chen[c], Alex Chinghuan Lee[c], Yanglong Hou[d], Ying Shirley Meng[e], Quan Li[a,*]

[a] Department of Physics, The Chinese University of Hong Kong, Shatin, New Territories, Hong Kong
[b] National Synchrotron Radiation Research Center, 101 Hsin-Ann Road, Hsinchu Science Park, Hsinchu, Taiwan
[c] Department of Mechanical and Automation Engineering, The Chinese University of Hong Kong, Shatin, New Territories, Hong Kong
[d] Department of Materials Science and Engineering, College of Engineering, Peking University, Beijing, PR China
[e] Department of Nano Engineering, University of California San Diego, 9500 Gilman Drive, La Jolla, CA 92093, USA

ARTICLE INFO

Keywords:
Fe_3O_4 nanoparticles
Graphene foam
Lithium ion batteries
Cycling performance

ABSTRACT

We identify that reversible formation/decomposition of lithium oxide, pulverization of Fe_3O_4 nanoparticles, and electrolyte reactions, are contributors to the enhanced capacity observed in the Fe_3O_4 electrode upon long cycling. Introducing three-dimensional graphene foam to form a composite with Fe_3O_4 nanoparticles largely increases the capacity (~ 1220 mA h g^{-1} vs. ~ 690 mA h g^{-1}) and promotes the cycling induced capacity enhancement (an earlier capacity rise and a faster rising rate) of the Fe_3O_4 electrode. Together with Fe_3O_4 nanoparticles, the presence of graphene effectively promotes the electrolyte reactions and reversible formation/decomposition of lithium oxide. At the same time, activation of GF also occurs in the presence of Fe_3O_4 nanoparticles, further increases the capacity of the nanocomposite.

1. Introduction

Magnetite (Fe_3O_4) is a promising electrode material for lithium ion batteries (LIBs) due to its high theoretical capacity (924 mA h g^{-1}), abundant material supply, environmental benignity, and low cost [1–6]. As Fe_3O_4 has a low electronic conductivity, it is commonly composited with conductive materials [4,5,7–14], for which graphene based materials are among the best choices. Examples include grafting bicontinuous mesoporous Fe_3O_4 nanostructure onto graphene foam (GF) [10] and Fe_3O_4 nanoparticles (NPs) anchored onto GF [13]. These electrodes exhibited high reversible capacity (800 mA h g^{-1} at 1 C [10]), fast charging and discharging capability (300 mA h g^{-1} at 20 C [13]), and good cycling stability (785 mA h g^{-1} at 1 C up to 500 cycles [10]).

It has been found that the capacity of the Fe_3O_4-based electrode usually shows a decrease during the initial cycles [10,13]. The capacity fading has been commonly attributed to the formation of unstable SEI layer [15]. On the other hand, cycling induced capacity increase has also been found in the Fe_3O_4-based electrode [10,13,14] after long cycles. Similar phenomenon has also been widely observed in other metal oxide electrodes upon long cycles [16–20]. The cycling enhanced capacity increase can be significant and stable [16], and its origin arouses much scientific interest. Much effort has been devoted to the search for possible reasons for the cycling dependent capacity change. Nevertheless, consensus has not been reached and the origin of the capacity change along with cycling remains unclear. One of the possible reasons is the lack of dynamic information directly related to the changes within the cells, due to the limited access to in-situ/operando experiments in many places. On the other hand, Fe_3O_4-based electrodes are usually composited with other additives, possible contribution from multiple factors makes it difficult to identify the origin.

In the present work, we first study the electrochemical performance of pure Fe_3O_4 trying to understand its cycling induced capacity change when excluding contribution from other material components. We have found that pure Fe_3O_4 electrode suffers from capacity fading in the first dozens of cycles, but experiences a capacity recovery/further rise then the capacity rises at a rate of ~ 1.4 mA h g^{-1} per cycle until it eventually stabilizes at ~ 690 mA h g^{-1}. Comprehensive study of the microstructure, electronic structure, and electrochemical characteristic evolution of the pure Fe_3O_4 electrode as a function of cycling reveals the origin of the capacity change as observed in pure Fe_3O_4 electrode. By introducing three-dimensional (3D) GF to form a nanocomposite with Fe_3O_4, we found further enhancement in the capacity and the cycling performance, that is, a rising rate of ~ 2.2 mA h g^{-1} per cycle,

---

* Corresponding author.
E-mail address: liquan@phy.cuhk.edu.hk (Q. Li).

http://dx.doi.org/10.1016/j.nanoen.2017.10.001
Received 4 July 2017; Received in revised form 31 August 2017; Accepted 1 October 2017

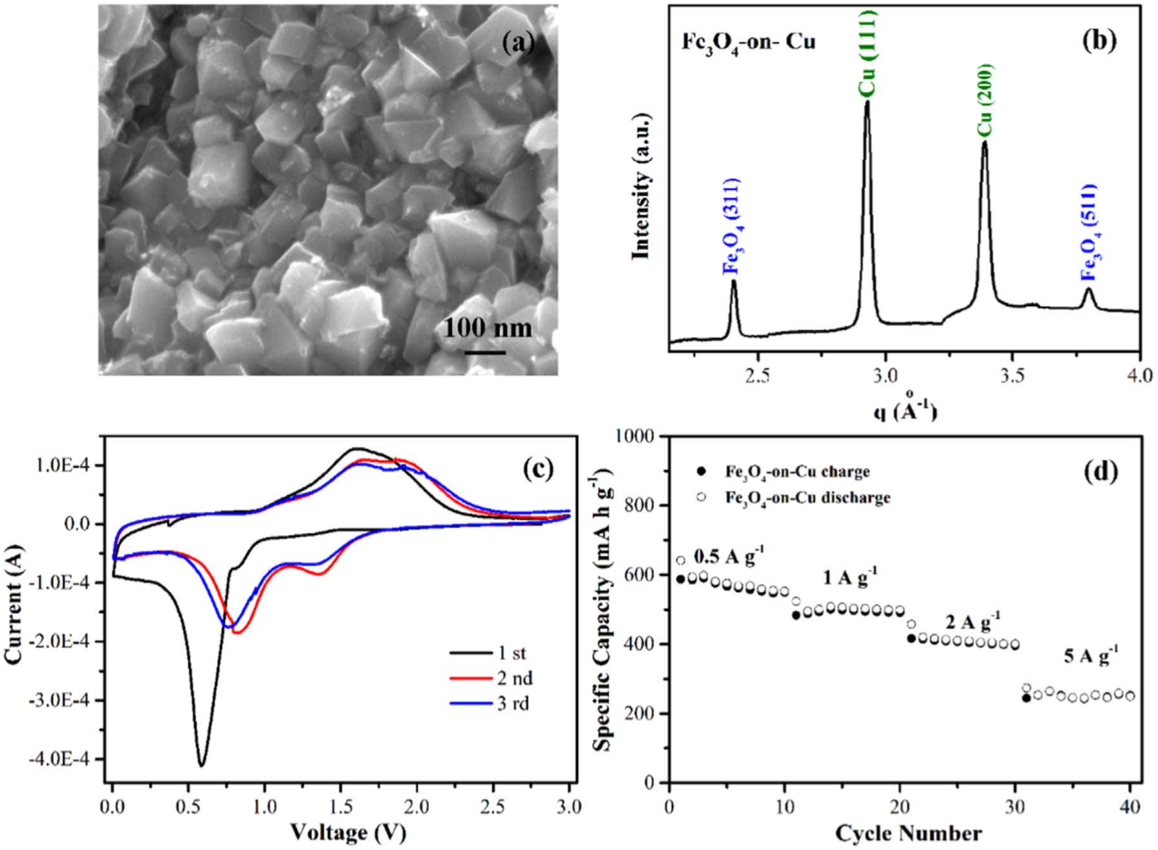

Fig. 1. (a) SEM image of the Fe_3O_4-on-Cu sample. (b) WAXS line integration of the original Fe_3O_4-on-Cu. (c) Cyclic voltammogram of Fe_3O_4-on-Cu at a scan rate of 0.1 mV s^{-1} in the voltage range of 0.01–3.0 V vs. Li^+/Li. (d) Specific capacities of Fe_3O_4-on-Cu samples at different rates.

and eventually stabilizing at ~ 1220 mA h g^{-1}. Multiple contribution of graphene as well as the synergistic effect of graphene and Fe_3O_4 in contributing to the cycling enhanced reversible capacity are elaborated.

2. Material and methods

2.1. Preparation of pure Fe_3O_4 electrode and GF-Fe_3O_4 nanocomposite

Fe_3O_4 was deposited on Cu foil by an electroplating process. A mixture consisting of 2 M NaOH, 0.09 M $Fe_2(SO_4)_3$·$5H_2O$ and 0.1 M triethanol-amine was used as electrolyte [21]. The Fe_3O_4 NPs were produced under stirring at 70 °C and a three-electrode set-up was used. A piece of Cu foil acted as the working electrode, whereas a Pt electrode served as the counter electrode. All potentials were quoted against an HgO/Hg° reference electrode. A current density of $-$ 5 mA cm^{-2} was applied to ensure coating of Fe_3O_4 on the Cu foil. After electroplating, the sample was carefully washed with deionized water to remove excess electrolyte and then dried in a vacuum oven overnight. The mass of deposited Fe_3O_4 was obtained by the weight difference of the samples before and after electroplating.

Graphene (6 carbon technology) was grown on Ni foam by chemical vapor deposition (CVD). Freestanding GF was obtained via etching off most of the Ni backbone in 2 M $FeCl_3$ solution at 50 °C and then washed by deionized water. In order to well control the GF during the electroplating process, 10 wt% of Ni was retained for obtaining the mechanically stable GF. The GF was vacuum dried overnight to remove the residual water. To determine the mass of the GF, the samples were weighed before and after CVD deposition.

Fe_3O_4 was deposited on GF by a similar electroplating process. A square-wave pulse current density of $-$ 5 mA cm^{-2} with a period of 0.25 s and a duty ratio of 0.625 was applied to ensure conformal coating of Fe_3O_4 on the GF.

2.2. Structure and morphology characterization

The morphology of the samples was characterized by a field-emission scanning electron microscope (FESEM, Quanta 200, FEI). TEM measurements were also carried out with a Tecnai F20 (FEI) microscope operating at 200 kV. Raman analysis was performed using a Micro Raman spectrometer (RM-1000, Renishaw Co., Ltd.) with a 10 mW helium-neon laser at 514 nm. The near edge X-ray adsorption fine structure (NEXAFS) experiments at the carbon K edge and oxygen K edge were conducted at the Beamline BL09A2 of the National Synchrotron Radiation Research Center located in Hsinchu, Taiwan. The NEXAFS experiments at the iron $L_{2,3}$ edge were conducted in X-ray fluorescence yield (FLY) mode on the BL27SU Beamline at SPring-8 in Japan. The Synchrotron wide angle X-ray scattering (WAXS) experiments were carried out at the BL23A1 X-ray Diffraction Beamline at National Synchrotron Radiation Research Center. The wavelength of incident beam was 0.0827 nm.

2.3. Electrochemical characterization

The electrochemical properties of the pure Fe_3O_4 electrode and GF-Fe_3O_4 nanocomposite were characterized by using CR2032 coin-type cells with Li foil as a counter electrode. The liquid electrolyte was 1.0 M $LiPF_6$ in the mixture of 1:1 (by volume) ethylene carbonate and diethyl carbonate (Novolyte Co.). In order to better understand the capacity contribution of GF in the GF-Fe_3O_4 nanocomposite, pure GF was also assembled to coin-type cells for measurement of the electrochemical properties. No binder or conducting additive was used in all of the electrodes. CV was conducted at a scanning rate of 0.1 mV s^{-1} between 0.01 and 3.0 V vs. Li^+/Li (CHI660, Shanghai CH Instrument Co., Ltd.). Galvanostatic charging/discharging cycles were tested between 0.01 and 3.0 V vs. Li^+/Li at different rates on a multichannel battery test system (CT2001A, Wuhan Kingnuo Electronic Co., Ltd.).

3. Results and discussion

3.1. Pure Fe_3O_4 electrode

Pure Fe_3O_4 electrode is fabricated via electroplating of Fe_3O_4 on Cu foil. The sample is denoted as Fe_3O_4-on-Cu. The SEM image discloses dense faceted particles of ~ 100 nm on the surface of copper (Fig. 1a). Synchrotron WAXS measurement of the same sample shows the diffraction signals of both Cu and Fe_3O_4 (Fig. 1b).

Fig. 1c shows the cyclic voltammetry (CV) of the Fe_3O_4-on-Cu samples at a scan rate of 0.1 mV s^{-1} in the voltage range of 0.01–3.0 V vs. Li^+/Li. A well-defined peak is observed at ~ 0.6 V in the first discharge cycle. The peak is generally ascribed to reduction of Fe^{3+} or Fe^{2+} to Fe° ($Fe_3O_4 + xLi^+ + xe^- \rightarrow Li_xFe_3O_4$, $Li_xFe_3O_4 + (8 - x)Li^+ + (8 - x)e^- \rightarrow 4Li_2O + 3Fe$) [5] and possible reaction with the electrolyte. Cathodic lithium insertion at ~ 0.8 and 1.4 V, and the anodic lithium extraction at 1.6 V are observed in the second and third cycles of Fe_3O_4-on-Cu samples, originated from electrochemical reduction/oxidation ($Fe_3O_4 \leftrightarrow Fe$) during lithiation/delithiation. To investigate the electrochemical performance of the Fe_3O_4-on-Cu sample, we conducted the galvanostatic discharge-charge measurements at various current densities (Fig. 1d). The Fe_3O_4-on-Cu sample exhibits a discharge capacity of ~ 593.6 mA h g^{-1} at low discharge rate of 0.5 A g^{-1}. Upon increasing discharge-charge rates to 1, 2, and 5 A g^{-1}, the reversible capacities are maintained at about 508.3, 413.4 and 265.3 mA h g^{-1}.

The discharge-charge cycling was performed at 1 A g^{-1} rate for 500 cycles (Fig. 2a). The Fe_3O_4-on-Cu electrode suffers from capacity fading in the first dozens of cycles. The specific capacity decreases from 501.4 (at the second cycle) to 412.5 mA h g^{-1} (at the 56th cycle). After that, the capacity of the Fe_3O_4-on-Cu electrode rises at a rate of ~ 1.4 mA h g^{-1} per cycle from ~ 180th cycle to ~ 320th cycle and eventually stabilizes at ~ 690 mA h g^{-1}. Fig. S1a (Supplementary material) presents the coulombic efficiency of the Fe_3O_4-on-Cu electrode during charge/discharge cycling. The coulombic efficiency of the Fe_3O_4-on-Cu in the first cycle is 77.59%. After the first few cycles, the coulombic efficiency of Fe_3O_4-on-Cu rises to 98.12–99.96%.

In order to understand the cycling induced capacity changes, Fe L-edge NEXAFS was performed in X-ray FLY mode on Fe_3O_4-on-Cu processed for different numbers of cycles, as shown in Fig. 2b. Fe L-edge NEXAFS spectra are dominated by a set of peaks around 709 eV (L_3, Fe $2p_{3/2}$ to Fe 3d transitions) and another set of peaks around 721 eV (L_2, Fe $2p_{1/2}$ to Fe 3d transitions). Due to the self-absorption effect, the L_3 peaks are highly distorted and we focus our discussion on L_2 line profiles. The L_2 peak is split into two peaks (the two labeled A_1 and A_2), due to the p-d Coulomb and exchange interactions, which represents the coordination of the Fe. Peak A_1 and peak A_2 appear at 721.6 and 723.1 eV, respectively. After the first discharge (sample 1 D), reduced Fe^{3+} or Fe^{2+} to Fe° leads to the disappearance of L_2 splitting and energy red shift to 720.9 eV, which is characteristic of Fe°. The split feature reappears after the first cycle (sample 1 C) and peak A_1 and A_2 are then blue-shifted to 721.4 and 723.4 eV, respectively, indicating oxidation of Fe° back to Fe^{3+} or Fe^{2+}. However, after 50 cycles (sample 50 C), splitting of the L_2 peaks become less obvious and a red-shift to 721.2 eV is observed. This suggests incomplete Fe° oxidation to Fe^{3+} or Fe^{2+} at 50 cycles. The presence of Fe° at the end of 50 cycles charged samples of Fe_3O_4-on-Cu suggests the incomplete redox reaction of Fe_3O_4 at early stage of the cycling, and thus provides an explanation to

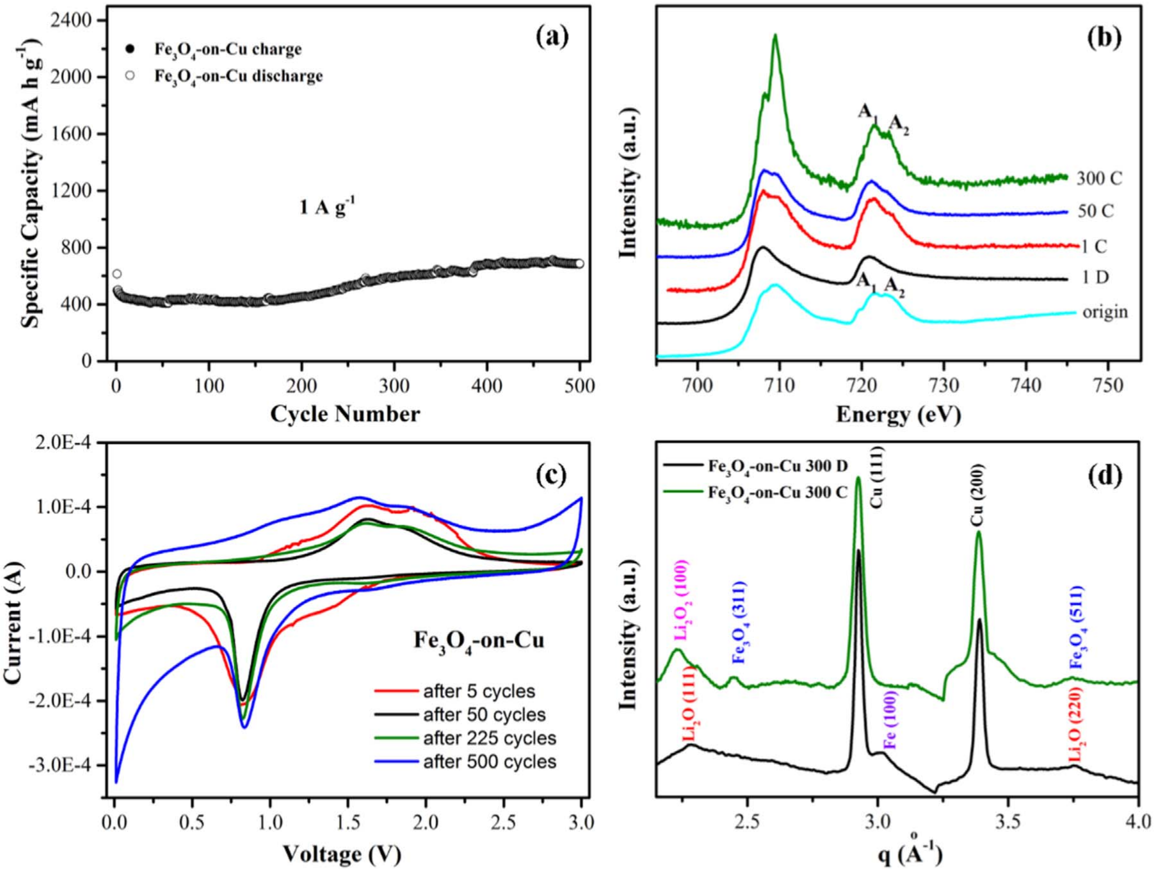

Fig. 2. (a) Cycling stability of Fe_3O_4-on-Cu cycled at a rate of 1 A g^{-1}. (b) Fe L-edge NEXAFS spectra for Fe_3O_4-on-Cu at different cycling stages. (c) Cyclic voltammogram of Fe_3O_4-on-Cu sample at a scan rate of 0.1 mV s^{-1} in the voltage range of 0.01–3.0 V vs. Li^+/Li after the 5, 50, 225, and 500 charge/discharge cycles. (d) Line integration of WAXS measurement of discharged Fe_3O_4-on-Cu and charged Fe_3O_4-on-Cu sample after 300 cycles.

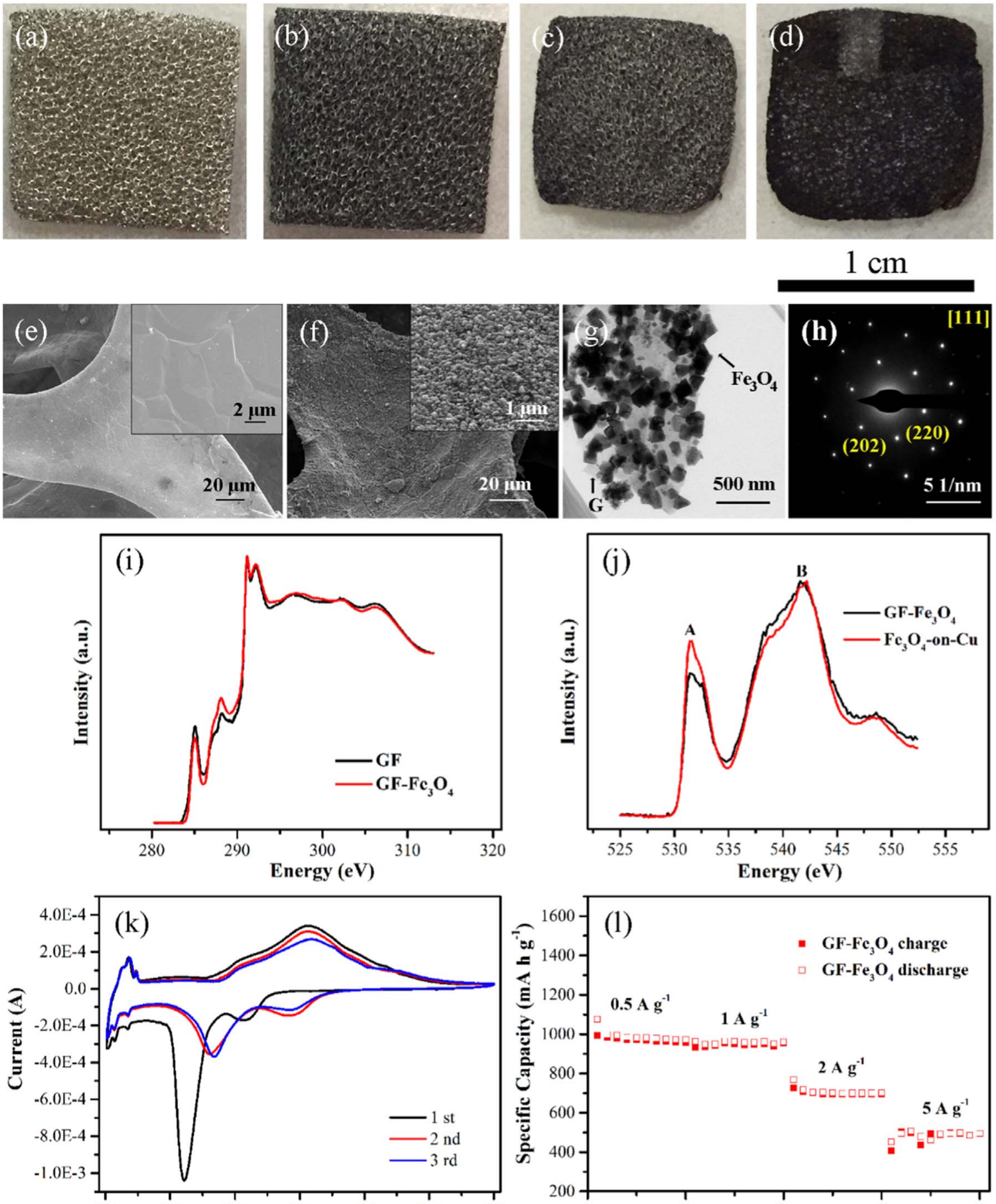

Fig. 3. Photographs of (a) Ni foam; (b) graphene deposited on Ni foam; (c) GF after 90 wt% Ni being etched off, and (d) Fe_3O_4 deposited on GF shown in Fig. 3c. (e) SEM image of CVD GF after 90 wt% Ni being etched. The high magnification image can be found in the inset. (f) SEM image of the GF-Fe_3O_4 nanocomposite. The high magnification image is in the inset. (g) TEM image taken from the GF-Fe_3O_4 nanocomposite sample. (h) SAED patterns of single Fe_3O_4 nanoparticle. (i) Carbon K edge NEXAFS spectra of GF and GF-Fe_3O_4 nanocomposite. (j) Oxygen K edge NEXAFS spectra of GF-Fe_3O_4 and Fe_3O_4-on-Cu samples. (k) Cyclic voltammogram of GF-Fe_3O_4 sample at scan rate of 0.1 mV s^{-1} in the voltage range of 0.01–3.0 V vs. Li$^+$/Li. (l) Specific capacities of GF-Fe_3O_4 samples at different rates.

the observed capacity decay recognized in the first dozens of cycles. Interestingly, a recovery of the L_2 edge line profile to that of the first cycle appears afterwards (sample 300 C).

The CVs (scanning rate of 0.1 mV s^{-1} in the voltage range of 0.01–3.0 V) of Fe_3O_4-on-Cu sample were also conducted at different cycles, aiming at disclosing the correlation between the cycling dependent electrode performance and the specific chemistry taking place. Fig. 2c compares the CV profiles of the Fe_3O_4-on-Cu sample taken after 5, 50 (before capacity increases), 225 (the beginning of the capacity rise), and 500 cycles. Compared to the CV profile of the Fe_3O_4-on-Cu sample after 5 cycles, the shape of the CV file after 50 cycles does not change significantly. However, an additional reduction peak below 0.02 V and an oxidation peak around 2.8–3.0 V appear at 225 charge/discharge cycles. These features become more prominent in the CV of Fe_3O_4-on-Cu sample after 500 cycles.

The large downturn below 0.02 V observed in the CVs of Fe_3O_4-on-

Cu sample after 500 cycles may result from the electrolyte reactions [22,23] or the Li plating, contributing to the capacity increase of the electrodes after long cycling. Nevertheless, SEM characterization of the discharged Fe_3O_4-on-Cu sample after 300 cycles does not suggest Li plating (Fig. S2, Supplementary material). This is consistent with the WAXS data obtained by synchrotron radiation (Fig. 2d)-no signal of Li metal ($q= \sim 2.53$) presents. Instead, the WAXS data reveals the presence of Li_2O and Fe, both of which are the expected products of the complete redox reaction at the end of discharge ($Fe_3O_4 + 8Li^+ + 8e^- \rightarrow 4Li_2O + 3Fe$). Therefore, the possibility of Li plating can be excluded.

The reaction corresponding to the upturn at ~ 2.8–3.0 V observed in the CVs of Fe_3O_4-on-Cu sample in Fig. 2c also contributes to the capacity increase after long cycling. This voltage range coincides with the oxidation voltage of lithium oxide decomposition ($2Li_2O \rightarrow Li_2O_2 + 2Li^+ + 2e^-$, $E = 2.87$ V [24]). The reaction of Li_2O to Li_2O_2 usually does not happen because Li_2O_2 can be highly insulating [25], automatically shut down the reaction. In fact, the WAXS pattern taken from the Fe_3O_4-on-Cu sample after 300 cycles does reveal the presence of Li_2O_2 at the end of charging (Fig. 2d). The experimental results suggest that the Fe_3O_4 acts as catalyst for such a reaction. The persistent and stable capacity increase after long cycling, as well as the corresponding CV data indicate the electrochemical reversibility of the lithium oxide formation/decomposition and the electrolyte reactions, serving as an important contributor to the cycling enhanced capacity of the Fe_3O_4 electrode. Comparing to the WAXS line integration of the as-fabricated Fe_3O_4-on-Cu sample (Fig. 1b), the peaks corresponding to Fe_3O_4 in Fe_3O_4-on-Cu after 300 cycles (Fig. 2d) broaden and decrease in intensity. This indicates that the Fe_3O_4 is pulverized, becoming nanocrystalline after 300 charge-discharge cycles. It is possible that the pulverization of Fe_3O_4 increases the surface area of the electrode and thus may release more active sites for lithium storage, as argued in the literature [10]. Nevertheless, similar observation of obvious capacity increase has been made in other materials systems [16–20], such as ultrafine MoO_2 nanoparticles (< 2 nm) based composite [18] and ultrafine MnO nanocrystals (< 3 nm) based composites [19], in which cases further pulverization of the crystals, if there is any, would not make significant change to the nanocrystals. In this regard, although we cannot completely exclude its contribution, pulverization of Fe_3O_4 nanoparticles is not likely to be a direct contributor that largely enhance the capacity of the electrode, that is to say, the capacity increase does not mainly come from the "newly generated reaction sites" on Fe_3O_4 due to its increased surface area as a result of particle pulverization. On the other hand, the large surface area associated with small nanoparticles can also promote its catalytic properties in enabling the reversible lithium oxide formation/decomposition.

3.2. GF-Fe_3O_4 nanocomposite electrode

Further enhancement in the capacity and the cycling performance of the Fe_3O_4 electrode can be achieved by introducing 3D GF to form a nanocomposite with Fe_3O_4. In such a sample, Fe_3O_4 is electrodeposited on 3D GF under the same experimental conditions as Fe_3O_4-on-Cu. The sample is denoted as GF-Fe_3O_4. Fig. 3a-d shows the morphology of the samples during the GF-Fe_3O_4 nanocomposite fabrication, from Ni foam (Fig. 3a) to graphene on Ni foam (Fig. 3b), to GF by etching off Ni (Fig. 3c), and to GF-Fe_3O_4 nanocomposite by electroplating Fe_3O_4 on GF (Fig. 3d). The mass loading of Fe_3O_4 is ~ 1.54 mg cm^{-2} and it takes 79.4% of the total mass of the nanocomposite.

The SEM image shown in Fig. 3e discloses the morphology of GF after etching off the Ni foam. It inherits the structure of the pristine Ni foam – a 3D porous network. After electroplating, the surface of GF becomes rough and dense particles can be seen on the surface (Fig. 3f). These particles can be seen in the high-magnification SEM image in the inset of Fig. 3f. Detailed structural characterizations of Fe_3O_4 NPs in the GF-Fe_3O_4 sample was carried out using TEM. Fig. 3g exhibits a representative TEM image of a piece of GF and Fe_3O_4 NPs. The sizes of the Fe_3O_4 NPs range from ~ 20 to ~ 180 nm, average at ~ 95 nm. The electron diffraction pattern taken from a single nanoparticle demonstrates the single-crystalline nature of individual Fe_3O_4 nanoparticle in the composite (Fig. 3h).

The structure of graphene has been examined using Raman spectroscopy, which data displays the degree of graphitization of carbon. As shown in Fig. S3 (Supplementary material), Raman spectrum of GF shows three typical peaks of graphene, centered at 1580, 2450, and 2720 cm^{-1}, corresponding to its G, G*, and 2D bands [26]. The G band is indicative of ordered graphitic crystallites of carbon (sp^2). Both the G* and 2D bands come from a two-phonon double resonance Raman scattering process. As a comparison, an additional peak centered at 667 cm^{-1} is observed in the Raman spectrum of the GF-Fe_3O_4 nanocomposite. It corresponds to the A_{1g} mode of Fe_3O_4 [10,13], originating from the symmetrical stretch of oxygen atoms along Fe-O bonds [27]. The disorder-induced D band at 1350 cm^{-1} does not appear in the Raman spectrum of either GF or GF-Fe_3O_4, owing to the high quality of the GF grown by CVD method.

NEXAFS was employed to probe possible changes in electronic structure of graphene and/or Fe_3O_4 before and after the nanocomposite was formed. Fig. 3i shows the carbon K edge NEXAFS spectra of the GF and GF-Fe_3O_4 nanocomposite. In a typical NEXAFS spectrum of GF, the peak at ~ 285.03 eV corresponds to the π^* transitions and those at 291.17 and 292.14 eV result from σ^* transitions [28–30]. The peak at 288.11 eV, corresponding to a 1s-π^* transition of carboxylic C, suggests the presence of a carboxylic group [29,31]. When the nanocomposite is formed, a similar carbon K edge spectrum is obtained. However, higher absorption intensity of the 288.11 eV transition is observed, implying charge transfer between the graphene and Fe_3O_4, via carboxylic groups. Consistent results are obtained when examining the oxygen K edge (Fig. 3j). Two peaks appear in the oxygen K edge spectra. The peak at 531.6 eV (A) is due to the electron transition from O 1s to the O 2p states hybridized with Fe 3d states [32]. The peak at 541.6 eV (B) is attributed to the transition to O 2p states hybridized with Fe 4sp states [32]. In the oxygen K-edge NEXAFS of GF-Fe_3O_4, an obvious decrease in unoccupied O 2p-Fe 3d hybridized state (peak A) is observed. This further confirms the presence of electron transfer from the carbon to the oxide via oxygen atoms in the GF-Fe_3O_4 nanocomposite [33].

The electrochemical performances of GF-Fe_3O_4 were investigated using half cells with lithium foils as counter electrodes. Fig. 3k show CV of the GF-Fe_3O_4 samples at a scan rate of 0.1 mV s^{-1} in the voltage range of 0.01–3.0 V vs. Li^+/Li. Apart from the redox reaction peaks for Fe_3O_4 which is also observed in the CV of Fe_3O_4-on-Cu (Fig. 1c), the CV profiles of GF-Fe_3O_4 nanocomposite show other pairs of redox peaks located at ~ 0.15 and ~ 0.20 V, which corresponds to the lithiation and delithiation of GF [10]. This pair of redox peaks are also observed in the cyclic voltammetry of the pure GF (Fig. S4, Supplementary material). To investigate the electrochemical performance of the GF-Fe_3O_4 nanocomposite, we conducted the galvanostatic discharge-charge measurements at various current densities (Fig. 3l). The GF-Fe_3O_4 sample delivers a discharge capacity of 991.8 mA h g^{-1} (based on the total mass of the GF-Fe_3O_4) at low current density of 0.5 A g^{-1}. A slight decrease in the discharging capacity is observed when the rate is increased to 1 A g^{-1}, and is kept at ~ 700.0 and ~ 500.0 mA h g^{-1} at further rate increase to 2, and 5 A g^{-1}, respectively. It is worth noting that GF also contributes to the measured capacity of GF-Fe_3O_4 nanocomposite at all rates. As shown in Fig. S5 (Supplementary material), GF exhibits a discharge capacity of ~ 280.9 mA h g^{-1} at 0.5 A g^{-1}. Even when the discharge current density increases to 5 A g^{-1}, GF still delivers a capacity of ~ 104.2 mA h g^{-1}. It is obvious that the GF-Fe_3O_4 sample exhibits much higher discharge capacity at various rates than Fe_3O_4-on-Cu. The introduction of GF contributes to the capacity enhancement of GF-Fe_3O_4 nanocomposite.

The introduction of GF is also found to bring additional improvement in the cycling enhanced capacity of Fe_3O_4. The discharge-charge

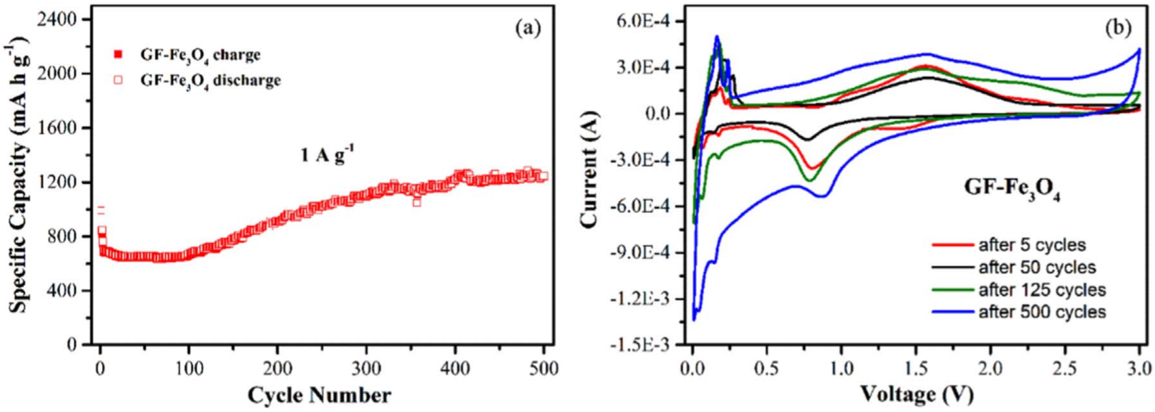

Fig. 4. (a) Cycling stability of GF-Fe$_3$O$_4$ cycled at a rate of 1 A g^{-1}. (b) Cyclic voltammogram of GF-Fe$_3$O$_4$ sample at scan rate of 0.1 mV s^{-1} in the voltage range of 0.01–3.0 V vs. Li$^+$/Li after the 5, 50, 125, and 500 charge/discharge cycles.

cycling of GF-Fe$_3$O$_4$ was performed at 1 A g^{-1} rate for 500 cycles (Fig. 4a). Similar to Fe$_3$O$_4$-on-Cu electrodes, the GF-Fe$_3$O$_4$ electrodes suffer from capacity fading in the first dozens of cycles and the capacity fading is attributed to incomplete redox reaction of Fe$_3$O$_4$ in the corresponding cycling rounds (Fig. S6, Supplementary material). After that, the capacity of the GF-Fe$_3$O$_4$ electrode rises at a rate of ~ 2.2 mA h g^{-1} per cycle from ~ 100th cycle to ~ 330th cycle, then stabilizes at ~ 1220 mA h g^{-1}. The occurrence of the capacity rise is earlier than that of the Fe$_3$O$_4$-on-Cu sample, and the rising rate is also greater when the GF is incorporated. The coulombic efficiency of the GF-Fe$_3$O$_4$ electrode during charge/discharge cycling is shown in Fig. S1b (Supplementary material). The coulombic efficiency of the GF-Fe$_3$O$_4$ in the first cycle is 71.60%. After the first few cycles, the coulombic efficiency of GF-Fe$_3$O$_4$ rises to 98.15–99.97%.

Ex-situ TEM characterizations of the GF-Fe$_3$O$_4$ samples were carried out at different cycles. TEM images taken from the GF-Fe$_3$O$_4$ samples after 1, 50, and 300 cycles (at the end of charging) are shown in Fig. S7a–c (Supplementary material). Compared to the TEM image (Fig. 3g) of the as-prepared GF-Fe$_3$O$_4$ sample (before cycling), the size of the Fe$_3$O$_4$ particles after 1 cycle and 50 cycles does not change significantly. Nevertheless, porous like structure starts to form right at the end of the first cycle. When the samples have been cycled for 300 runs, obvious reduction of the Fe$_3$O$_4$ particles size to ~ 20 nm can be observed, although these small sized particles remain crystalline (as shown in Fig. S7d, Supplementary material). Pulverization of the Fe$_3$O$_4$ is obvious after 300 charge-discharge cycles.

CV of GF-Fe$_3$O$_4$ were also conducted after 5, 50 (before capacity increase), 125 (the beginning of the capacity increase), and 500 cycles (Fig. 4b). After 50 cycles, the shape of the CV file remains similar to the result of after 5 cycles. Similar to that of the Fe$_3$O$_4$-on-Cu sample, an additional reduction peak below 0.02 V and an oxidation peak around 2.8–3.0 V are observed after 125 cycles. At the end of 500 cycles, these features become more prominent. Similar chemistry holds for reactions correlated with the large downturn below 0.02 V (likely due to electrolyte reactions), and the upturn at ~ 2.8–3.0 V ($2Li_2O \rightarrow Li_2O_2 + 2Li^+ + 2e^-$). Evidence of the Li$_2$O presence is also found in the line integration of WAXS measurement of discharged GF-Fe$_3$O$_4$ after 300 cycles (Fig. S8a, Supplementary material). The signal of Li$_2$O$_2$ is observed in both the selected area diffraction (Fig. S9, Supplementary material) and the line integration of WAXS measurement of charged GF-Fe$_3$O$_4$ after 300 cycles (Fig. S8b, Supplementary material), suggesting that reversible formation and decomposition of lithium oxide occur during the charge-discharge cycles. Such changes are absent in the CV of the pure GF electrode after cycling (Fig. S10b, Supplementary material), further confirming the important role of Fe$_3$O$_4$ in the electrolyte reactions and decomposition of lithium oxide. The fact that such reactions appear earlier in the GF-Fe$_3$O$_4$ (after 125 cycles) than in the Fe$_3$O$_4$-on-Cu (after 225 cycles), reveals the participation of GF (together with Fe$_3$O$_4$) in promoting the corresponding reaction.

On the other hand, a distinctive difference exists between the CV profiles of the GF-Fe$_3$O$_4$ and that of the Fe$_3$O$_4$-on-Cu sample. A significant current increase appear in both the reduction peak around 0.15 V (due to the lithiation of GF) and the oxidation peaks around 0.2 V (due to the delithiation of GF) after 500 cycles in the GF-Fe$_3$O$_4$ sample. Although the fact that the 0.15 V peak residing on the slope of the large downturn below 0.02 V makes it arguable on the actual magnitude of the reduction current increase associated with the GF lithiation process, a distinctive > 2 time increase in the oxidation current associated with the GF delithiation suggests activation of GF in the cycling in the presence of Fe$_3$O$_4$. It also contributes to the larger capacity increase rate of GF-Fe$_3$O$_4$ sample as compared to Fe$_3$O$_4$-on-Cu. It is noted that such high increase does not appear in the long cycling of pure GF (Fig. S10a, Supplementary material) and a distinctive increase in the oxidation/reduction current associated with the GF delithiation/lithiation is absent in the CVs of GF after 500 cycles (Fig. S10b, Supplementary material), suggesting the activation of GF only takes place in the GF-Fe$_3$O$_4$ nanocomposite.

Cycling induced capacity increase has been reported in Fe$_3$O$_4$ based electrode materials as well as in some other metal oxide systems [10,16–20]. Efforts have been paid to understand the cycling dependent capacity change for possible applications in a broader range, and a few hypotheses were made, including enhanced conductivity of the electrode due to the generation of Fe nanoparticles, the increased surface area resulted from the pulverization of Fe$_3$O$_4$, and the decomposition of the electrolyte [10]. Nevertheless, conflicts exist in the literature and the origin of the capacity increase remains arguable. In the present work, we exclude the presence of Fe° as a contributor to the capacity increase after long cycles, as the presence of Fe° actually coincides with a drop in the capacity after 50 cycles and it eventually disappears after 300 cycles (suggested by the Fe L-edge NEXAFS taken from Fe$_3$O$_4$-on-Cu and GF-Fe$_3$O$_4$ nanocomposite processed for different numbers of cycles (Figs. 2b and S6)). The observation of the large downturn below 0.02 V in the CVs of the sample (Figs. 2c and 4b) supports the hypotheses of electrolyte reactions. The broadened diffraction signal of the Fe$_3$O$_4$ particles after 500 cycles (Fig. 2d) and the obvious reduction of the Fe$_3$O$_4$ particles size after 300 cycles (Fig. S7c) support the hypotheses of Fe$_3$O$_4$ pulverization as a possible contributor to the capacity increase. Nevertheless, experimental evidence of increased capacity of ultrafine MoO$_2$ nanoparticles (< 2 nm) based composite [18] and ultrafine MnO nanocrystals based composites [19] have been shown in literature, In these cases, further pulverization makes little change to the nanoparticles. The results suggest direct contribution from pulverization of Fe$_3$O$_4$ nanoparticles to the capacity enhancement of the electrode is low. Thus, there are other contributors to the capacity increase after long cycling. In the present work, we give experimental evidence of reversible formation and decomposition of lithium oxide as well as activation of GF in the cycling of GF-Fe_3O_4, which factors serve as important contributors to the capacity increase after long cycling.

Although electrolyte reaction is not encouraged in a battery, the observed reversible formation and decomposition of Li_2O_2 upon cycling is a key issue for the Li-O_2 cells [34]. Much effort has been made to develop effective electrocatalysts that enable the reaction reversibility, which is critical to the development of rechargeable Li-O_2 cells. The present study suggests that the Fe_3O_4 NPs contribute to the reversible formation/decomposition of Li_2O_2, and the participation of GF (together with Fe_3O_4) further promotes such reactions. These findings will inspire the mechanistic study of the above-mentioned catalytic reaction, leading to new designs/development of the electrocatalysts for the Li-O_2 cells.

4. Conclusion

In conclusion, we show that pure Fe_3O_4 electrode suffers from capacity fading in the first dozens of cycles, after which the capacity rises at a rate of ~ 1.4 mA h g^{-1} per cycle until it eventually stabilizes at ~ 690 mA h g^{-1}. Experimental evidence suggests that reversible formation/decomposition of lithium oxide serves as a major contributor to the enhanced capacity upon long cycling. More significant capacity increase (a climbing rate of ~ 2.2 mA h g^{-1} per cycle) upon cycling are obtained when 3D GF is introduced to form a nanocomposite with Fe_3O_4. We find that participation of GF (together with Fe_3O_4) effectively promotes the electrolyte reactions and decomposition of lithium oxide. At the same time, activation of GF is achieved in the presence of Fe_3O_4, further contributing to the capacity increase of GF-Fe_3O_4 sample as compared to that of pure Fe_3O_4 electrode. Our finding will shed new light on understanding the electrochemistry of nano-scale metal-oxide, guiding new architecture design of nano metal-oxides based electrodes. The discovery of GF-Fe_3O_4 promoting the reversible formation and decomposition of Li_2O_2 may inspire research and development of electrocatalysts for the Li-O_2 cells.

Acknowledgements

This work is supported by a research fund of the National Natural Science Foundation of China/Research Grants Council Joint Research Scheme under Project no. N_CUHK448/13. The synchrotron radiation experiments at Spring-8 were performed on the BL27SU Beamline with the approval of the Japan Synchrotron Radiation Research Institute (JASRI) (Proposal no. 2016A1039). The authors are grateful to Dr. Y. Tamenori of JASRI/SPring-8 for his support. Technical support from National Synchrotron Radiation Research Center in Taiwan and the Shanghai Synchrotron Radiation Facility are gratefully acknowledged. The authors are grateful to YC Lu for stimulating discussions.

Appendix A. Supplementary material

Supplementary data associated with this article can be found in the online version at http://dx.doi.org/10.1016/j.nanoen.2017.10.001.

References

[1] Z.-W. Zhao, T. Wen, K. Liang, Y.-F. Jiang, X. Zhou, C.-C. Shen, A.-W. Xu, Carbon-coated Fe_3O_4/VO_x hollow microboxes derived from metal-organic frameworks as a high-performance anode material for lithium-ion batteries, ACS Appl. Mater. Interfaces 9 (2017) 3757–3765.

[2] M. Liu, H. Jin, E. Uchaker, Z. Xie, Y. Wang, G. Cao, S. Hou, J. Li, One-pot synthesis of in-situ carbon-coated Fe_3O_4 as long-life lithium-ion battery anode, Nanotechnology 28 (2017) 155603, http://dx.doi.org/10.1088/1361-6528/aa6143.

[3] J. Liu, X. Xu, R. Hu, L. Yang, M. Zhu, Uniform hierarchical Fe_3O_4@polypyrrole nanocages for superior lithium ion battery anodes, Adv. Energy Mater. 6 (2016) 1600256.

[4] Q. An, F. Lv, Q. Liu, C. Han, K. Zhao, J. Sheng, Q. Wei, M. Yan, L. Mai, Amorphous vanadium oxide matrixes supporting hierarchical porous Fe_3O_4/graphene nanowires as a high-rate lithium storage anode, Nano Lett. 14 (2014) 6250–6256.

[5] L. Li, A. Kovalchuk, H. Fei, Z. Peng, Y. Li, N.D. Kim, C. Xiang, Y. Yang, G. Ruan, J.M. Tour, Enhanced cycling stability of lithium-ion batteries using graphene-wrapped Fe_3O_4-graphene nanoribbons as anode materials, Adv. Energy Mater. 5 (2015) 1500171.

[6] Y. Dong, Z. Zhang, Y. Xia, Y.-S. Chui, J.-M. Lee, J.A. Zapien, Green and facile synthesis of Fe_3O_4 and graphene nanocomposites with enhanced rate capability and cycling stability for lithium ion batteries, J. Mater. Chem. A 3 (2015) 16206–16212.

[7] J. Zhang, K. Wang, Q. Xu, Y. Zhou, F. Cheng, S. Guo, Beyond yolk-shell nanoparticles: Fe_3O_4@Fe_3C core@shell nanoparticles as yolks and carbon nanospindles as shells for efficient lithium ion storage, ACS Nano 9 (2015) 3369–3376.

[8] Y. Zuo, G. Wang, J. Peng, G. Li, Y. Ma, F. Yu, B. Dai, X. Guo, C.-P. Wong, Hybridization of graphene nanosheets and carbon-coated hollow Fe_3O_4 nanoparticles as a high-performance anode material for lithium-ion batteries, J. Mater. Chem. A 4 (2016) 2453–2460.

[9] L. Zhao, M. Gao, W. Yue, Y. Jiang, Y. Wang, Y. Ren, F. Hu, Sandwich-structured graphene-Fe_3O_4@carbon nanocomposites for high-performance lithium-ion batteries, ACS Appl. Mater. Interfaces 7 (2015) 9709–9715.

[10] J. Luo, J. Liu, Z. Zeng, C.F. Ng, L. Ma, H. Zhang, J. Lin, Z. Shen, H.J. Fan, Three-dimensional graphene foam supported Fe_3O_4 lithium battery anodes with long cycle life and high rate capability, Nano Lett. 13 (2013) 6136–6143.

[11] W. Zhang, X. Li, J. Liang, K. Tang, Y. Zhu, Y. Qian, One-step thermolysis synthesis of two-dimensional ultrafine Fe_3O_4 particles/carbon nanonetworks for high-performance lithium-ion batteries, Nanoscale 8 (2016) 4733–4741.

[12] J. Zhao, B. Yang, Z. Zheng, J. Yang, Z. Yang, P. Zhang, W. Ren, X. Yan, Facile preparation of one-dimensional wrapping structure: graphene nanoscroll-wrapped of Fe_3O_4 nanoparticles and its application for lithium-ion battery, ACS Appl. Mater. Interfaces 6 (2014) 9890–9896.

[13] X. Hu, M. Ma, M. Zeng, Y. Sun, L. Chen, Y. Xue, T. Zhang, X. Ai, R.G. Mendes, M.H. Rümmeli, L. Fu, Supercritical carbon dioxide anchored Fe_3O_4 nanoparticles on graphene foam and lithium battery performance, ACS Appl. Mater. Interfaces 6 (2014) 22527–22533.

[14] W. Wei, S. Yang, H. Zhou, I. Lieberwirth, X. Feng, K. Müllen, 3D graphene foams cross-linked with pre-encapsulated Fe_3O_4 nanospheres for enhanced lithium storage, Adv. Mater. 25 (2013) 2909–2914.

[15] C. He, S. Wu, N. Zhao, C. Shi, E. Liu, J. Li, Carbon-encapsulated Fe_3O_4 nanoparticles as a high-rate lithium ion battery anode material, ACS Nano 7 (2013) 4459–4469.

[16] H. Sun, G. Xin, T. Hu, M. Yu, D. Shao, X. Sun, J. Lian, High-rate lithiation-induced reactivation of mesoporous hollow spheres for long-lived lithium-ion batteries, Nat. Commun. 5 (2014) 4526.

[17] Y. Liu, J. Xu, X. Qin, H. Xin, X. Yuan, J. Zhang, D. Li, C. Song, Electrode activation via vesiculation: improved reversible capacity of γ-Fe_2O_3@C/MWNT composite anodes for lithium-ion batteries, J. Mater. Chem. A 3 (2015) 9682–9688.

[18] Y. Sun, X. Hu, W. Luo, Y. Huang, Ultrafine MoO_2 nanoparticles embedded in a carbon matrix as a high-capacity and long-life anode for lithium-ion batteries, J. Mater. Chem. 22 (2012) 425–431.

[19] F. Zheng, G. Xia, Y. Yang, Q. Chen, MOF-derived ultrafine MnO nanocrystals embedded in a porous carbon matrix as high performance anodes for lithium-ion batteries, Nanoscale 7 (2015) 9637–9645.

[20] H. Sun, L. Mei, J. Liang, Z. Zhao, C. Lee, H. Fei, M. Ding, J. Lau, M. Li, C. Wang, X. Xu, G. Hao, B. Papandrea, I. Shakir, B. Dunn, Y. Huang, X. Duan, Three-dimensional holey-graphene/niobia composite architectures for ultrahigh-rate energy storage, Science 356 (2017) 599–604.

[21] P.L. Taberna, S. Mitra, P. Poizot, P. Simon, J.-M. Tarascon, High rate capabilities Fe_3O_4-based Cu nano-architectured electrodes for lithium-ion battery applications, Nat. Mater. 5 (2006) 567–573.

[22] S. Laruelle, S. Grugeon, P. Poizot, M. Dollé, L. Dupont, J.-M. Tarascon, On the origin of the extra electrochemical capacity displayed by MO/Li cells at low potential, J. Electrochem. Soc. 149 (2002) A627–A634.

[23] S. Grugeon, S. Laruelle, L. Dupont, J.-M. Tarascon, An update on the reactivity of nanoparticles Co-based compounds towards Li, Solid State Sci. 5 (2003) 895–904.

[24] S. Okuoka, Y. Ogasawara, Y. Suga, M. Hibino, T. Kudo, H. Ono, K. Yonehara, Y. Sumida, Y. Yamada, A. Yamada, M. Oshima, E. Tochigi, N. Shibata, Y. Ikuhara, N. Mizuno, A new sealed lithium-peroxide battery with a Co-doped Li_2O cathode in a superconcentrated lithium bis(fluorosulfonyl)amide electrolyte, Sci. Rep. 4 (2014) 5684.

[25] L. Zhong, R.R. Mitchell, Y. Liu, B.M. Gallant, C.V. Thompson, J.Y. Huang, S.X. Mao, Y. Shao-Horn, In situ transmission electron microscopy observations of electrochemical oxidation of Li_2O_2, Nano Lett. 13 (2013) 2209–2214.

[26] A. Kumar, M.R. Maschmann, S.L. Hodson, J. Baur, T.S. Fisher, Carbon nanotube arrays decorated with multi-layer graphene-nanopetals enhance mechanical strength and durability, Carbon 84 (2015) 236–245.

[27] O.N. Shebanova, P. Lazor, Raman spectroscopic study of magnetite ($FeFe_2O_4$): a new assignment for the vibrational spectrum, J. Solid State Chem. 174 (2003) 424–430.

[28] D. Wang, J. Yang, X. Li, D. Geng, R. Li, M. Cai, T.-K. Sham, X. Sun, Layer by layer assembly of sandwiched graphene/SnO_2 nanorod/carbon nanostructures with ultrahigh lithium ion storage properties, Energy Environ. Sci. 6 (2013) 2900–2906.

[29] D. Wang, X. Li, J. Yang, J. Wang, D. Geng, R. Li, M. Cai, T.-K. Sham, X. Sun, Hierarchical nanostructured core–shell Sn@C nanoparticles embedded in graphene nanosheets: spectroscopic view and their application in lithium ion batteries, Phys. Chem. Chem. Phys. 15 (2013) 3535–3542.

[30] S.-W. Lee, S.-M. Bak, C.-W. Lee, C. Jaye, D.A. Fischer, B.-K. Kim, X.-Q. Yang, K.-W. Nam, K.-B. Kim, Structural changes in reduced graphene oxide upon MnO_2

deposition by the redox reaction between carbon and permanganate ions, J. Phys. Chem. C 118 (2014) 2834–2843.

[31] B. Singh, Y. Fang, B.C.C. Cowie, L. Thomsen, NEXAFS and XPS characterisation of carbon functional groups of fresh and aged biochars, Org. Geochem. 77 (2014) 1–10.

[32] D.N. Mueller, M.L. Machala, H. Bluhm, W.C. Chueh, Redox activity of surface oxygen anions in oxygen-deficient perovskite oxides during electrochemical reactions, Nat. Commun. 6 (2015) 6097.

[33] J. Liu, J. Liu, W. Song, F. Wang, Y. Song, The role of electronic interaction in the use of Ag and Mn_3O_4 hybrid nanocrystals covalently coupled with carbon as advanced oxygen reduction electrocatalysts, J. Mater. Chem. A 2 (2014) 17477–17488.

[34] W. Fan, Z. Cui, X. Guo, Tracking formation and decomposition of abacus-ball-shaped lithium peroxides in Li-O_2 cells, J. Phys. Chem. C 117 (2015) 2623–2627.